A-PRIORI INFORMATION DRIVEN DETECTION OF MOVING OBJECTS FOR TRAFFIC MONITORING BY SPACEBORNE SAR

Franz Meyer[†], Stefan Hinz[‡], Andreas Laika[‡], Richard Bamler[†,‡]

[†]Remote Sensing Technology Institute, German Aerospace Center (DLR)
Oberpfaffenhofen, D - 82234 Wessling, Germany
[‡]Remote Sensing Technology, Technische Universitaet Muenchen
Arcisstr. 21, D - 80333 Muenchen, Germany

Commission III, WG III/5

KEY WORDS: Traffic Monitoring, SAR, Satellite Images

ABSTRACT

This paper derives the theoretical background for upcoming dual-channel radar satellite missions to monitor traffic from space. As it is well-known, an object moving with a velocity deviating from the assumptions incorporated in the focusing process will generally appear both displaced and blurred in azimuth direction. To study the impact of these (and related) distortions in focused SAR images, the analytic relations between an arbitrary moving point scatterer and its conjugate in the SAR image have been derived and adapted to dual-channel satellite specifications. To be able to monitor traffic under these boundary conditions in real-life situations, a specific detection scheme is proposed. This scheme integrates complementary detection and velocity estimation algorithms with knowledge derived from external sources as, e.g., road databases.

1 INTRODUCTION

During the past years, increasing traffic appears to be one of the major problems in urban and sub-urban areas. On one hand, the increase of transport safety and transport efficiency and, on the other hand, the reduction of air and noise pollution are the main tasks to solve in the future. Traffic monitoring has consequently evolved as an important research issue.

Since the launch of new optical satellite systems, satellite imagery with 1-meter resolution or higher is commercially available and a number of approaches have been developed to detect or track vehicles in this imagery (see e.g. references in (Leitloff et al., 2005), these proceedings). Traffic monitoring based on optical satellite systems, however, is only possible at daytime and cloud-free imagery. Spaceborne SAR (Synthetic Aperture Radar) systems bypass these limitations. Yet there are other difficulties inherent in the SAR imaging process that must be overcome to design a reasonable good approach for traffic monitoring using spaceborne radar. It is the focus of this paper to thoroughly analyze and quantify these effects and to develop an approach that is capable to detect vehicles travelling strictly on streets and roads and to estimate their velocity, thereby considering the restrictions of *civilian* SAR satellite systems.

We exemplify our approach by the upcoming TerraSAR-X mission. Its high resolution synthetic aperture radar sensor operates in X-band and delivers images of 1–3m resolution. The system can be switched to an experimental split-antenna mode, which acquires two high resolution SAR images of the same scene within a small time frame. Especially this split-antenna mode is going to provide data suited for traffic monitoring. The relevant system parameters and notations are summarized in Table 1.

2 MOVING OBJECTS IN SAR IMAGES

2.1 Object Motion Effects in TerraSAR-X Data

The position of a radar transmitter on board of a satellite is given by $P_{sat}(t) = [x_{sat}(t), y_{sat}(t), z_{sat}(t)]$. A point scatterer is assumed to be at $P_{mover} = [x_{mover}(t), y_{mover}(t), z_{mover}(t)]$. The range to an arbitrarily moving and accelerating point target from the radar platform is defined by $R(t) = |P_{sat}(t) - P_{mover}(t)|$ and the measured echo signal of this point scatterer can consequently be written as

orbit height	h	515,000 m
wavelength	λ	0.0311 m
satellite velocity	v_{sat}	7,600 m/s
beam velocity on ground	v_B	7,105 m/s
range (@ 40 degrees)	R_0	670,000 m
FM rate	FM	- 5183 Hz/s
processed Doppler bandwidth	PBW	3000 Hz
processed synthetic aperture	T_A	0.5788 s
Pulse repetition frequency	PRF	4000 Hz
Ground sampling distance		1-3 m

Table 1: Parameters of the TerraSAR-X satellite.

$$u(t) = a_\theta(\theta) \cdot a_\beta(\beta) \cdot g(\tau - 2R/c) \cdot \exp\{-j\frac{4\pi}{\lambda} \cdot R(t)\} \quad (1)$$

with τ and t being fast and slow time, respectively, $g(\tau - 2R/c)$ being the delayed complex pulse envelope, and $a_\theta(\theta)$, $a_\beta(\beta)$ being the amplitude of the two-way antenna patterns in elevation and azimuth, respectively (Bamler and Schättler, 1993). For further investigations the amplitude $A = a_\theta(\theta) \cdot a_\beta(\beta) \cdot g(\tau - 2R/c)$ is set to 1 to simplify the equations.

Azimuth focussing of the SAR image is done using the matched filter concept. According to this concept the filter must correspond to

$$s(t) = \exp\{j\frac{4\pi}{\lambda} \cdot R(t)\} \quad (2)$$

in order to give an optimally focussed image. To compute the matched filter correctly, the real range history to each target in the image must be simulated. For this, a priori information about sensor and scatterer position and motion in necessary. Usually, the time dependence of the scatterer position is ignored yielding $P_{mover}(t) = P_{mover}$. Additionally, in the case of spaceborne SAR, $\exp\{-j\frac{4\pi}{\lambda} \cdot R(t)\}$ is often approximated by $\exp\{j\pi FMt^2\}$ with $FM = -\frac{2}{\lambda}\frac{d^2}{dt^2}R(t)$ being the frequency modulation rate of the azimuth chirp accounting for satellite motion only. This concept is commonly referred to as *stationary-world matched filter* (SWMF). Per definition a SWMF does not correctly represent the phase history of a moving object resulting in image deteriorations.

2.1.1 Azimuth Displacement due to Across-Track Motion The target should now move with velocity v_{y0} in across-track direction. This movement causes a change of range history proportional to the projection of the motion vector into the line-of-sight direction of the sensor $v_{los} = v_{y0} \cdot sin(\theta)$, with θ being the local elevation angle. In case of constant motion during illumination the change of range history is linear and causes an additional linear phase trend in the echo signal. The resulting signal of an object moving in line-of-sight direction with velocity v_{los} is consequently:

$$u(t) = \exp\{j\pi FMt^2\} \cdot \exp\{-j\frac{4\pi}{\lambda}v_{los}t\} \quad (3)$$

The spectrum $T(f) = U(f) \cdot S(f)$ of the moving target after focusing with a matched filter of the form (in time-domain)

$$s(t) = \exp\{-j\pi FMt^2\} \quad . \quad (4)$$

results in

$$T(f) = \exp\left\{-j2\pi\frac{2}{\lambda FM}fv_{los}\right\}\exp\left\{-j2\pi\frac{2}{\lambda^2 FM}v_{los}^2\right\} \quad (5)$$

As one can see, $T(f)$ is composed of a linear phase (first part) and a constant phase term (second part). Following the laws of Fourier transform the linear phase component corresponds to a *time shift t_{shift} in time domain*. Fourier-transforming the linear term of Equation (5) yields:

$$t_{shift} = \frac{2v_{los}}{\lambda FM} \quad [s]. \quad (6)$$

Some simple transformations of Equation (6) give the *azimuth displacement of a moving object in space domain*

$$\Delta_{azimuth} = -R\frac{v_{los}}{v_{sat}} \quad [m] \quad (7)$$

with $t_{shift} = \frac{\Delta_{azimuth}}{v_B}$ where v_B is the beam velocity on ground. Across-track motion consequently results in an along-track displacement of the moving object. It is displaced in flying direction if the object moves towards the sensor (i.e. the range decreases) and reverse to flying direction if the movement is directed away from the sensor (i.e. the range increases). As the range R is defined by $R = \frac{h_{sat}}{cos(\theta)}$ the azimuth shift is strongly dependent on the viewing angle θ.

Based on Equation (7) and on Table 1 the azimuth shift of a target moving with velocity v_{y0} in across-track is calculated for the TerraSAR-X case. The results are presented in Figure 1.

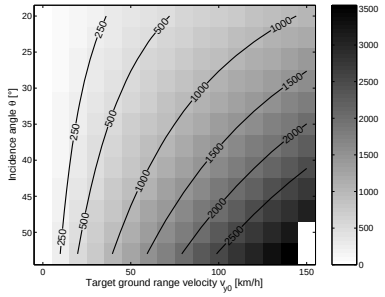

Figure 1: Azimuth displacement of a moving object in meter as function of θ and v_{y0}

As can be seen, moving vehicles imaged by TerraSAR-X are displaced significantly from their real position even for small across-track velocities (about $1\,km$ for $50\,km/h$ at $45°$ inc. angle). This effect strongly hampers the recognition of cars in TerraSAR-X images as their position is not related to semantic information, e.g. streets. Figure 1 also shows that the azimuth displacement is ambiguous if the doppler shift $\Delta f_d = \frac{2v_{los}}{\lambda}$ introduced by the target's motion in line-of-sight exceeds $\Delta f_d > \frac{PRF}{2}$ or $v_{y0} > \pm\frac{PRF\lambda}{4\sin\theta}$. This effect can be observed in the lower right corner of Figure 1. There, the across-track velocity of the object rises above the ambiguity limit. As a consequence the object is wrapped around the frequency band and appears at the position of the ambiguity (negative displacement).

2.1.2 Signal Blurring due to Along-Track Motion The target is now assumed to move with velocity v_{x0} in azimuth direction (along-track). The relative velocity of sensor and scatterer is different for the moving object and the surrounding stationary world. Thus, along track motion changes the frequency modulation (FM) rate FM_{mt} of the received scatterer response. The FM rate of a target moving in along-track direction with velocity v_{x0} is given by

$$FM_{mt} = FM\left(1 - \frac{v_{x0}}{v_B}\right) \quad (8)$$

The received signal of a target moving in along track and its associated spectrum can be written as

$$u_{mt}(t) = \exp\{j\pi FM_{mt}t^2\} \quad (9)$$

$$U_{mt}(f) = \exp\{-j\pi\frac{f^2}{FM_{mt}}\} \quad (10)$$

The product of the spectra $T_{mt}(f) = U_{mt}(f) \cdot S(f)$ corresponds to the convolution in time domain and results in

$$T_{mt}(f) = \exp\left\{-j\pi\frac{f^2}{\delta FM}\right\} \quad . \quad (11)$$

where

$$\frac{1}{\delta FM} \approx -\lambda\sqrt{\frac{v_{sat}}{v_B}}\frac{v_{x0}}{(v_{sat}v_B)^{\frac{3}{2}}}R \quad (12)$$

The phase of the focused signal $T_{mt}(f)$ is quardatic and causes a spreading of the signal energy in time or space domain depending on δFM. Unfortunately, the Fourier transform of $T_{mt}(f)$ has no analytic solution. Nevertheless, considering the stationary phase approximation the width of the focused peak can be approximated by

$$\Delta t \approx \frac{PRF}{\delta FM} = 2T_A\sqrt{\frac{v_{sat}}{v_B}}\frac{v_{x0}}{\sqrt{v_{sat}v_B}} \quad [s] \quad (13)$$

with T_A being the aperture time. Interpretation of Equation (13) shows that *a moving vehicle is smeared by twice the distance it moved along-track during the illumination time T_A*. It has to be kept in mind that the approximation in Equation (13) only holds if $v_{x0} \gg 0$.

As the backscattered energy of the moving object is now spread over a larger area the peak value of the signal drops down with increasing v_{x0}. The signal amplitude at position $t = 0$ (the position of the signal peak) can be calculated by integrating the signal spectrum.

$$h(0; v_{az}) = \int_{-PRF/2}^{PRF/2}\exp\left\{j\pi\lambda\sqrt{\frac{v_{sat}}{v_B}}\frac{v_{x0}}{(v_{sat}v_B)^{\frac{3}{2}}}Rf^2\right\}df \left[\frac{1}{s^2}\right] \quad (14)$$

To solve Equation (14) analytically, we make use of the stationary phase approximation. Hence, the signal amplitude calculates to

$$h(0; v_{x0}) \approx \delta FM = \frac{1}{\lambda\sqrt{\frac{v_{sat}}{v_B}}R}\frac{(v_{sat}v_B)^{\frac{3}{2}}}{v_{x0}} \quad (15)$$

The decrease of peak power in TerraSAR-X images as a function of the along-track velocity is illustrated in Figure 2. As can be seen, the effect of along-track movement has significant influence on the peak amplitude in TerraSAR-X images. Strong

blurring distributes the backscattered energy and results in a drop of $50\,\%$ peak power or more if $v_{x0} \geq 14.4\,km/h$. Consequently, nearly all ground moving targets will suffer from energy dispersion, which decreases the signal-to-clutter ratio and renders target detection more difficult if tried to be detected with a SWMF.

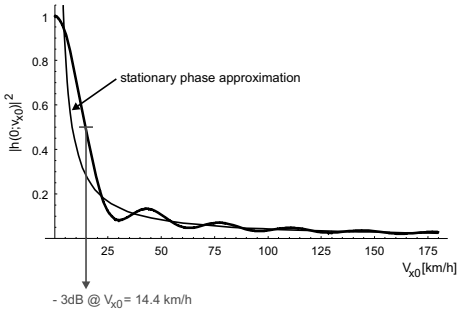

Figure 2: Decrease of peak power with v_{x0} in TerraSAR-X SLCs.

2.1.3 Effects due to Object's Acceleration In the majority of GMTI literature, it is assumed that vehicles travel with constant velocity and along a straight path (Gierull, 2004, Livingstone et al., 2002). If vehicle traffic on roads and highways is monitored, target acceleration is commonplace and must be considered in any processor or realistic simulation. Acceleration effects do not only appear when drivers physically accelerate or break but also due to curved roads, since the object's along-track and across-track velocity components vary during the radar illumination.

Let a radar transmitter on board of a satellite at the altitude H move with constant velocity v_{sat} in along-track direction (x-axis). The point scatterer is assumed to be at position $(0, y_0, 0)$ at azimuth time $t = 0$ and to move with velocity components v_{x0} and v_{y0} and acceleration components a_x and a_y in along-track and across-track direction, respectively. The vehicle's height is assumed to be zero over the entire observation period and the vehicle is assumed to be non-rotating. R_0 is the slant rage at azimuth time $t = 0$ and $R(t)$ represents the range from the radar to the target as any time t.

The third order Taylor series expansion of the range to an accelerating point target from the radar platform is given as (Sharma and Collins, 2004):

$$\begin{aligned} R(t) = R_0 + \frac{y_0 v_{y0}}{R_0} t + \\ \frac{1}{2R_0}\left[(v_{x0} - v_{sat})^2 + v_{y0}^2\left(1 - \frac{y_0^2}{R_0^2}\right) + y_0 a_{y0}\right] t^2 + \\ \frac{1}{2R_0}\left[y_0 a_{y0}\left(1 - \frac{y_0^2}{R_0^2}\right) + (v_{x0} - v_{sat}) a_{x0}\right] t^3 - \\ \frac{1}{2R_0}\left[\frac{y_0 v_{y0}(v_{x0} - v_{sat})^2 + y_0 v_{y0}^3}{R_0^2}\right] t^3 \end{aligned} \quad (16)$$

It can be seen in Equation (16) that acceleration components appear in the quadratic and the cubic term of the Taylor series expansion. The *acceleration in across-track direction* (a_y) causes a quadratic phase component in the range equation which results in a spreading of the signal energy in time or space domain depending on the targets across-track acceleration. Considering the TerraSAR-X system parameters given in Table 1 the amount of defocussing in TerraSAR-X images is calculated as a function of *across-track acceleration*. Figure 3 gives an impression off the amount of blurring that has to be expected for accelerations that commonly occur in vehicle traffic on roads or highways. It can be seen from Figure 3 that image degradation due to across-track accelerations is significant for $a_y > 1\,\frac{m}{s^2}$.

Along-track acceleration a_x appears in the cubic term of the range equation and results in an asymmetry of the focused point spread function. For TerraSAR-X the deformation of the point spread function is very small even for very strong and very unrealistic acceleration values. For typical accelerations in common traffic scenarios ($a_x < 2\,\frac{m}{s^2}$) the effect is nearly zero.

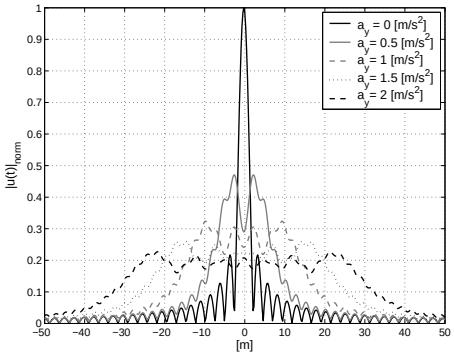

Figure 3: Broadening of the point spread function as a function of a_y in TerraSAR-X SLCs.

3 APPROACH TO DETECTION AND VELOCITY ESTIMATION OF MOVING OBJECTS

On one hand, effects of moving objects hinder the detection of cars in conventionally processed SAR images. On the other hand, these effects are mainly deterministic and thus can be exploited to not only detect vehicles but also measure their velocity. The main tasks to accomplish this are the *estimation* of blurring and displacement (or equivalently, the interferometric phase of two co-registered images). The solution to this typical inverse problem can be eased when incorporating a priori knowledge about the appearance, location, and velocity of vehicles.

Our scheme for vehicle detection and velocity estimation relies on three basic components: (1) The integration of a priori knowledge (Sect. 3.1); (2) a Constant False Alarm Rate (CFAR) detector operating on along-track interferometric data to estimate the across-track velocity component (Sect. 3.2); and (3) an algorithm for estimating the along-track velocity component based on frequency modulation rate variation (Sect. 3.3).

3.1 Integration of A Priori Knowledge

Assuming objects being point scatterers and given the SAR- and platform parameters, the displacement effect in along-track direction due to an objects across-track motion can be predicted when real position, velocity, and motion direction of the mover are known. Because of the functional relation of interferometric phase and object velocity in across-track direction, also the interferometric phase of a (displaced) moving object can be derived. These types of prediction may be interpreted as a priori knowledge that can be acquired, analyzed and stored independent of image acquisition.

In our case, road network databases serve as basic source for acquiring a priori knowledge. Typically, these databases contain road axes in form of polygons and attributes like road class, road width, maximum velocity, etc. attached to each polygon. Using this information a number of "maps" representing the a priori information can be derived (i.e. displacement map, velocity map, and interferometric phase map).

Besides the information about the phase, also a priori information about the vehicle's radar cross section strongly supports detection. As it is well known, significant variations of radar cross section exist over different aspect angles of cars. Typical variations are derived from simulations and experimental measurements. Such information can also be incorporated into the detection scheme with the help of a road database, since - given the sensor and platform parameters - the aspect angle under which a car must have been illuminated by the sensor can be calculated for each road segment.

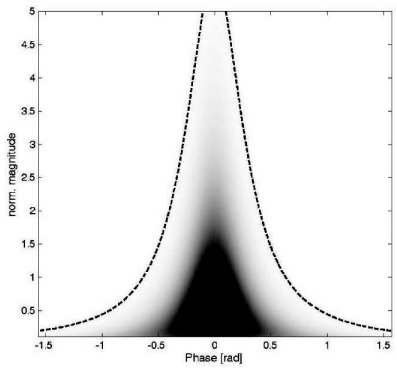

Figure 4: Theoretical joint probability density function $f_c(\eta, \psi)$ of single-look interferometric phase and magnitude normalized to $E[\eta] = 1$. Coherency is set to $|\rho| = 0.95$. The dashed line is an example for a curve of separation.

3.2 ATI Constant False Alarm Rate Detector

In the case of along-track interferometry (ATI) an interferogram I is formed from the original complex data sets I_1 and I_2. For all stationary targets the interferometric phase values $\psi = (\varphi_1 - \varphi_2)$ will be distributed around the expectation value $E[\psi] = 0$. The joint probability density function (pdf) $f_c(\eta, \psi)$ of amplitude and phase of an interferogram has been derived in (Lee et al., 1994) and (Joughin et al., 1994) using the underlying assumption of jointly Gaussian-distributed data in the two images. It is given by:

$$f_c(\eta,\psi) = \frac{2n^{n+1}\eta^n}{\pi\Gamma(n)\left(1-|\rho|^2\right)} \exp\left(\frac{2n\eta\,|\rho|\cos(\psi)}{1-|\rho|^2}\right) \cdot K_{n-1}\left(\frac{2n\eta}{1-|\rho|^2}\right) \quad (17)$$

where n is the number of looks, $\Gamma(\bullet)$ is the gamma function and $K_n(\bullet)$ is the modified Bessel function of the nth kind. As a precondition for the validity of the pdf it was assumed that $E[\eta] = 1$. Multilooking is done by averaging over n pixels assuming stationarity. For medium resolution SAR the jointly Gaussian assumption has been validated in most agricultural and heavily vegetated areas.

Figure 4 shows a typical example of the pdf assuming a coherency of $|\rho| = 0.95$, $n = 1$ and a expected signal amplitude of $E[\eta] = 1$. The pdf is centered on a phase value of $\psi = 0$ as expected.

Based on this pdf a constant false alarm rate (CFAR) detector can be designed that groups all image pixels into two classes. Class 1, called "clutter only", contains all pixels that only carry image information. Class 2, called "no clutter", contains all pixels that are not part of the image pdf. This class 2 includes pixels that contain moving vehicles but also all sort of outliers. Since the pdf of this second class is not known, it is assumed to be equally distributed over a large area. With this assumption we can compute a likelihood ratio. Classification is done by comparing that likelihood ratio with thresholds α. This approach provides curves of separation between the two classes, which are actually isolines on $f_c(\eta, \psi)$.

An example of a possible curves of separation is indicated in Fig. 4 by black dashed lines. The chosen curve of separation determines the probability of false alarm (P_{fa}); sometimes also referred to as "'false alarm rate"' (FAR). It is simply the integral of the Clutter pdf over the area where $f_c(\eta, \psi) < \alpha$.

Applying a CFAR detector of the given design for detecting vehicles is optimal only in cases when amplitude and phase of a possible moving target in an arbitrary image pixel is uniformly

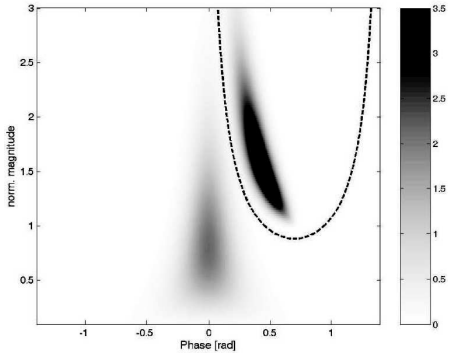

Figure 5: Theoretical joint PDF of the alternative hypotheses and its position relative to the hypotheses "Clutter only". The dashed line is an example for an improved curve of separation.

distributed. This holds for many military applications, where vehicles are not bound to roads and can move in any arbitrary direction. In case of public traffic, where a priori information about position, velocity and movement direction of vehicles is available to a certain degree, the use of a simple CFAR detector is suboptimal. As outlined in Sect. 3.1 it is possible to derive expectation values for position, velocity (i.e. interferometric phase), and aspect-dependent radar cross section of vehicles using ancillary data. In the following, we integrate these data into the ATI-CFAR detector.

The moving target signal is assumed to have a peak amplitude β and a phase shift ϑ. The Parameter β is proportional to the square root of the radar cross section σ. A new class describing the superposition of moving target signal and clutter, called 'vehicle & clutter' can be introduced now. The Class 'vehicle & clutter' is a subset of the class 'no clutter'. Unfortunately a pdf $f_{c+m}(\eta, \psi)$ describing the probability density of this class has not been found yet. An approximation, valid for $n >> 1$ has been derived in (Gierull, 2002). This approximation $f_{c+m}(\eta, \psi)$ is given by:

$$f_{c+m}(\eta,\psi) = \frac{2n^{n+1}\eta\left(\left(\eta-\delta\cos(\psi-\vartheta)\right)^2+\delta^2\sin(\psi-\vartheta)^2\right)^{\frac{n-1}{2}}}{\pi\Gamma(n)\left(1-|\rho|^2\right)} \cdot \exp\left(\frac{2n\rho\left(\eta\cos(\psi)-\delta\cos(\vartheta)\right)}{1-\rho^2}\right) \cdot K_{n-1}\left(\frac{2n\sqrt{\left(\eta-\delta\cos(\psi-\vartheta)\right)^2+\delta^2\sin(\psi-\vartheta)^2}}{1-\rho^2}\right) \quad \text{with } \delta = \frac{\beta}{\eta} \quad (18)$$

Using this approximation as an alternative hypothesis $f_{c+m}(\eta, \psi)$ allows to define a new likelihood ratio. Again thresholds can be applied resulting in new curves of separation. These lines are not isolines anymore, but they separate the class 'vehicle & clutter' much better from the class 'clutter only'. Thus the risk of falsely detecting an outlier is reduced and P_{FA} is decreased. Figure 5 shows an example of the shape of $f_{c+m}(\eta, \psi)$ and its position relative to the hypotheses 'clutter only'. An example of a curve of separation is also given. It encloses the class 'vehicle & clutter' much better than the one in Fig. 4. The incorporation of a priori information into the vehicle detector improves the amount of detected targets and also reduces the number of false alarms. But, in order to define the 'vehicle & clutter' pdf external data sources are indispensable that allow to obtain the necessary a priori information about the vehicles impulse response β and the vehicles interferometric phase ϑ.

To evaluate the quality of this approach, an ATI CFAR simulator has been implemented whose output are Receiver Operator

Characteristics (ROC) Curves (Laika et al., 2005). This simulator can be parameterized in such a way that a priori information about the interferometric phase and amplitude can be integrated or omitted. Hence, the benefits of integration a priori information can be quantified.

To evaluate the performance of the two detectors with and the detector without a priori information the detection threshold threshold α is varied and the probability of detection and probability of false alarm are determined for each step of this variation, eventually resulting in ROC-curves. Figures 6 and 7 show the ROC-curves of the two detectors for different signal-to-clutter ratios (Fig. 6) and for different number of looks (Fig. 7). The comparison of the two ATI detectors shows a clear advantage for the one using a priori knowledge. Especially in bad detection scenarios the improvements tend to be larger.

Once a vehicle has been detected with this algorithm, there exist two complementary ways to estimate its across-track velocity: (1) 2π-multiples of the interferometric phase measured in this particular pixel; an (2) the displacement of this from the corresponding road. The second measure is much more accurate, yet it might be ambiguous in case of a very dense road network when a displaced car can be re-projected onto more than one road. The first measure is less accurate and also ambiguous by multiples of the interferometric phase. However, since the interferometric phase can be transformed into a displacement value, it can be interpreted as a likelihood function indicating the probability of a particular road section being the true corresponding road. Hence, the interferometric phase helps to robustly resolve potential ambiguities in velocity estimation based on displacement. Having established the match of detected vehicle and its corresponding road section, also the along-track velocity component can be computed via simple trigonometry.

3.3 FM Rate Variation Detector

The approach outlined so far can only be applied if displacement occurs at all. This does not happen for objects moving purely in along-track direction. Hence, in this section, we turn to the estimation of along-track velocity.

The main reason for blurred imaging of moving point scatterers is a wrongly assumed FM rate in the SWMF caused by neglecting the objects along-track velocity. However, focusing moving objects is in fact possible when choosing the correct FM rate during matched filter design. Our strategy for finding the correct relative velocity relies on hypothesizing a series of FM rates and analyzing a pixel's "sharpness function", eventually yielding the correct estimate of the along-track velocity. The known location of roads as well as the expected range of vehicle velocities allow to restrict the search space (see also (Gierull and Sikaneta, 2004)).

Figure 8a) illustrates a stack of differently focused SAR-images and a slice along a certain azimuth line to be analyzed. Figure 8b) shows the typical shape of the sharpness function for a moving point scatterer in this slice in real data and Fig. 8c) the same but analytical and noise-free function. For stationary points, the energy peak of the sharpness function would come up along the slice's central row. The faster an object moves, the more the energy peak deviates from this row. This effect can be seen, for instance, in Fig. 8b). As a consequence of this observation, the algorithm must be able to find the energy peak of the potentially Speckle-disturbed sharpness function. The distance from the central row to the found point gives immediately the estimate of the along-track velocity.

For extracting the energy peak, we implemented a simple but effective blob detection scheme that analyzes the local curvatures in azimuth- and FM-direction (see Fig. 8c), thereby incorporating a certain amount of smoothing depending on the expected noise level of the images. Combining local curvature maxima and energy amplitude by the geometric mean yields the final decision function, from which the maximum is selected.

Summarizing this section, our system is based on two complementary algorithms, one for detection and velocity estimation using across-track phenomena and the other using along-track phenomena. Both are optimized using a priori knowledge derived from ancillary data and they are linked via information about the road network.

4 EXPERIMENTS AND VALIDATIONS

In order to verify the validity of the theory, a flight campaign has been conducted to compare the theoretical derivations with real data. This test also enables to discover bottlenecks of the techniques employed and to reveal unforeseen problems. An additional goal of the flight campaign is to simulate TerraSAR-X data for predicting the performance of the extraction procedures. To this end, an airborne radar system has been used with a number of modifications, so that the resulting raw data is comparable with the future satellite data. Please note that the following experiments are not intended to yield an in-depth performance characterization of our approach when applied to different real-life traffic scenarios. In fact, such experiments will be carried out during 2005. This first campaign was motivated by the need to proof, validate, and possibly improve theory and simulations with help of controlled conditions.

During the campaign 8 controlled vehicles moved along the runway of an airfield. All vehicles were equipped with a GPS system with a 10 Hz logging frequency for measuring their position and velocity. Some small vehicles were equipped with corner reflectors to make them visible in the image. 6 GMTI experiments with varying angle between the heading of the aircraft and the vehicles, have been flown. The vehicles have been moved with such velocities that they approximately match traffic scenarios as recorded by satellites.

In order to verify the theory, the predicted image position of a moving object is derived from the object's GPS position and its

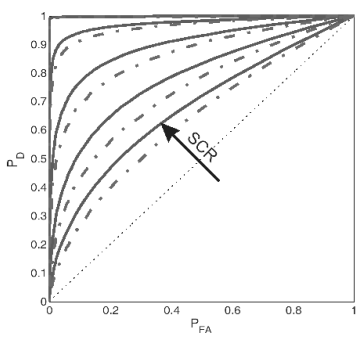

Figure 6: Performance of an ATI-detector using a priori information (solid line) compared to an ATI-detector using no a priori information (dashed line) for signal to clutter ratios of (innermost to outermost) -3dB, 0dB, 3dB, 6dB and 10dB (single look).

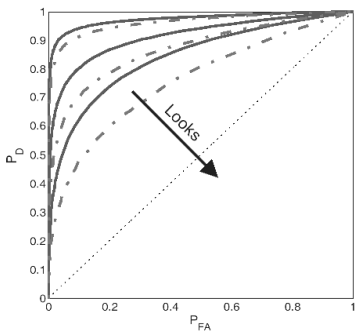

Figure 7: Performance of an ATI-detector using a priori information (solid line) compared to an ATI-detector using no a priori information (dashed line) for different numbers of looks(signal to clutter ratio fixed at 6db). From outermost to innermost: 1 look, 3 looks, 9 looks.

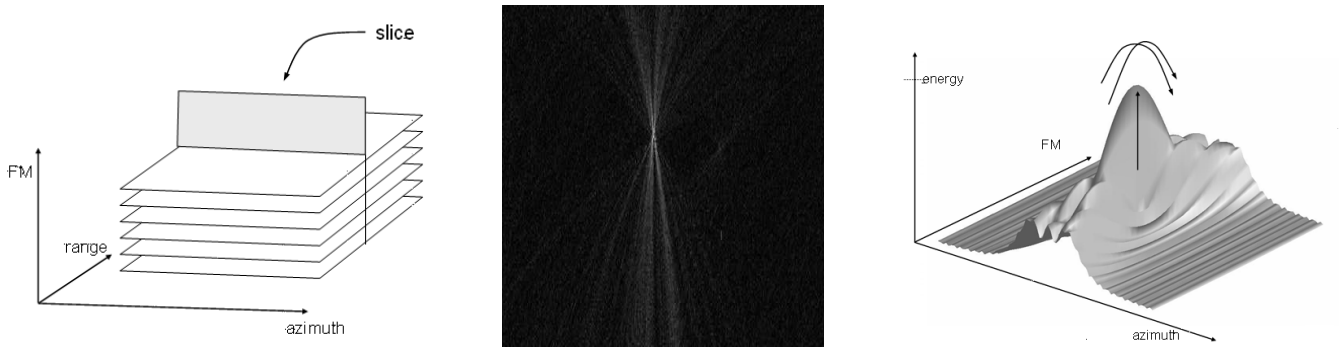

(a) Slice through differently focused SAR images. (b) Sharpness function of moving object in slice. (c) Analytical sharpness function.

Figure 8: 2D-slice along azimuth line through stack of SAR images, focused with different FM rates.

measured velocity. This position is compared to the position measured in the image. To get quantitative estimates of the quality of velocity determination from TerraSAR-X images, the velocity corresponding to the along-track displacement in the SAR images has been compared to the GPS velocity. Results of this comparison are given in (Suchandt et al., 2005).

Figure 9 illustrates the validation of the ATI experiments. In Fig. 9a) the positions of displaced vehicles detected in the image (yellow dots) are compared with their true GPS-position (green dots) and the theoretical displacement computed from the GPS-velocities (red dots). As can be seen, yellow and red dots match very well, so that the theoretical background of detection and velocity estimation seems justified. Other experiments are shown in Figs. 9b) and c). Here, the interferometric phases of two detected vehicles (red rectangles) have been measured and the vehicles have been re-projected onto the corresponding road section (red arrows). The velocity derived from the projection yields $133\,km/h$ and $130\,km/h$, respectively. Both velocities are reasonable for this section of the highway and, moreover, match closely 2π-multiples of their corresponding interferometric phase values.

Although there might be some inaccuracies included in the measurements (varying local incidence angle, GPS-time synchronization, etc.) the results show a very good match of theory and real measurements. As expected target 7 is not visible in the image. This is due to the low PBW of only 1/10 of the PRF and the targets velocity. The across-track velocity of target 7 shifts the spectrum of the target outside of the PBW which is centered around $f_{dc} = 0$. This is another indication for the appropriate mathematical modelling in Section 2.

ACKNOWLEDGEMENT

This work has been partly founded by the DLR project TerraSAR-X Traffic Products. The support of our project team, especially Hartmut Runge, Steffen Suchandt, and Michael Eineder, is gratefully acknowledged.

REFERENCES

Bamler, R. and Schättler, B., 1993. SAR Data Acquisition and Image Formation. In: G. Schreier (ed.), Geocoding: ERS-1 SAR Data and Systems, Wichmann-Verlag.

Gierull, C., 2002. Moving Target Detection with Along-Track SAR Interferometry. A Theoretical Analysis. Technical Report DRDC-OTTAWA-TR-2002-084, Defence R&D Canada.

Gierull, C., 2004. Statistical Analysis of Multilook SAR Interferograms for CFAR Detection of Ground Moving Targets. IEEE Transactions on Geoscience and Remote Sensing 42, pp. 691–701.

Gierull, C.-H. and Sikaneta, I., 2004. Ground Moving Target Parameter Estimation for Two-Channel SAR. In: Proc. Of EUSAR04.

Joughin, I., Winebrenner, D. and Percival, D., 1994. Probability density functions for multilook polarimetric signatures. IEEE Transactions on Geoscience and Remote Sensing 32(2), pp. 562–574.

Laika, A., Meyer, F., Hinz, S. and Bamler, R., 2005. Incorporating a priori Knowledge into a Moving Vehicle Detector for TerraSAR-X Data. In: International Archives of Photogrammetry, Remote Sensing and Spatial Information Sciences, Vol. 36(8/W27).

Lee, J.-S., Hoppel, K., Mango, S. and Miller, A., 1994. Intensity and phase statistics of multilook polarimetric and interferometric SAR imagery. IEEE Transactions on Geoscience and Remote Sensing 32(5), pp. 1017–1028.

Leitloff, J., Hinz, S. and Stilla, U., 2005. Automatic Vehicle Detection in Space Images Supported by Digital Map Data. In: ISPRS/DAGM joint Workshop on City Models, Road Databases, and Traffic Monitoring, CMRT05, Vienna.

Livingstone, C.-E., Sikaneta, I., Gierull, C.-H., Chiu, S., Beaudoin, A., Campbell, J., Beaudoin, J., Gong, S. and Knight, T.-A., 2002. An Airborne Sythentic Apertur Radar (SAR) Experiment to Support RADARSAT-2 Ground Moving Target Indication (GMTI). Canadian Journal of Remote Sensing 28(6), pp. 794–813.

Sharma, J. and Collins, M., 2004. Simulation of SAR Signals from Moving Vehicles (Focusing Accelerating Ground Moving Targets). In: Proc. Of EUSAR04.

Suchandt, S., Palubinskas, G., Runge, H., Eineder, M. and Meyer, F., 2005. An Airborne SAR Experiment for Ground Moving Target Identification. In: Proc. of Workshop on High-Resolution Earth Imaging for Geospatial Information, Hanover.

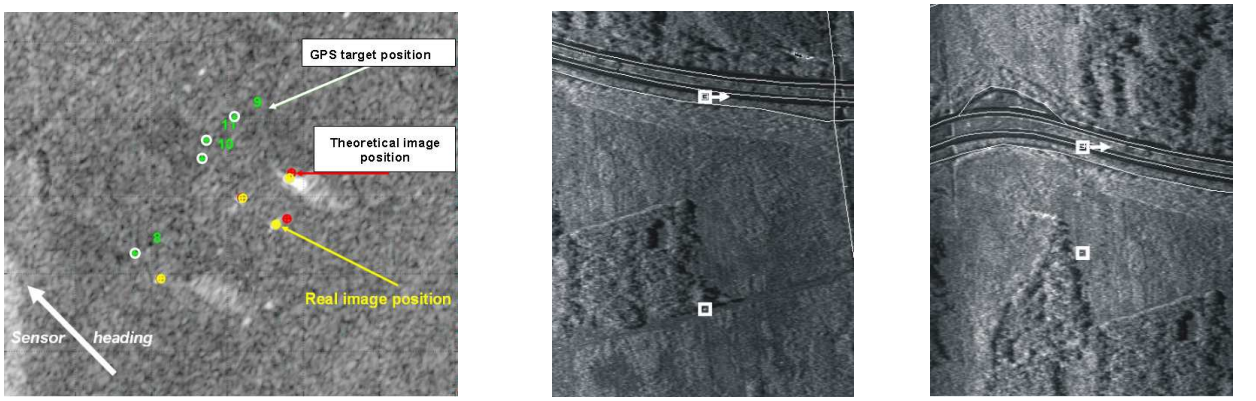

(a) Validation of displacement effects. (b) left, (c) right: Velocity estimation using road data, displacement, and phase values.

Figure 9: Experiments with airborne SAR.